Nanoscale

PAPER

View Article Online
View Journal | View Issue

Cite this: *Nanoscale*, 2024, **16**, 7443

Er^{3+}-activated $Ba_2V_2O_7$ upconversion nanosheets for dual-mode temperature sensing†

Satish Kumar Samal, Sahana Kulkarni, Jyoti Yadav and Boddu S. Naidu *

Received 15th December 2023,
Accepted 6th March 2024

DOI: 10.1039/d3nr06401h

rsc.li/nanoscale

So far, there has been substantial research on non-contact luminescence thermometry approaches that rely on luminescence intensity ratio (LIR) technology. However, there is limited availability of phosphors doped with Er^{3+} ions that exhibit on-par luminescence and high sensitivity. In this work, samples of $Ba_2V_2O_7$:Er^{3+} were synthesized using a sol–gel method aided by citric acid. The luminescence properties of these samples, including upconversion and down-shifting, were investigated using both ultraviolet and 980 nm laser stimulation. When subjected to ultraviolet (UV) light, the sample exhibits a distinct broad-band emission that appears pale green. This emission is a distinguishing property of the sample and is attributed to the presence of $V_2O_7^{2-}$ ions. Upon being stimulated by a 980 nm laser, the sample exhibits standard green up-conversion Er^{3+} emission bands. Concurrently, an assessment was conducted on the phosphor's ability to measure temperature by analysing the LIR between the thermally coupled $^2H_{11/2}$, $^4S_{3/2}$ energy levels (TCELs) and the non-thermally coupled $^2H_{11/2}$, $^4F_{9/2}$ energy levels (NTCELs) of the Er^{3+} ion. The corresponding highest sensitivity of temperature for TCELs and NTCELs can position $Ba_2V_2O_7$:Er^{3+} nanosheets as a capable option for materials utilized in temperature-sensing applications.

1. Introduction

Temperature measurement is critical in many fields, including healthcare, industry, research and technology. Temperature sensors have traditionally been used to monitor temperature; however, these sensors frequently need contact with the object being measured, making them inappropriate for some applications. But, with the introduction of optical thermometry, temperature measuring has become more flexible and precise. Optical thermometry is a non-contact method of measuring temperature that uses infrared (IR) radiation generated by an object to calculate its temperature. The increasing popularity of this technology may be attributed to its several benefits, including its high level of accuracy, extensive temperature range, rapid operation, and non-contact characteristics. These attributes make it well-suited for a broad range of applications across multiple sectors.[1–3] Based on emission peak wavelength or peak width, luminescence intensity ratio (LIR), and lifetime of luminescence, various luminescent materials have been devised as temperature-sensing materials used in optical thermometers, of which those based on the LIR technique are widely used due to their ability to eliminate excitation source variation as well as fluorescence loss. The LIR approach capitalizes on the inconsistencies in the responses to temperature of two emission signals resulting from TCELs of transition metals or rare-earth (RE) ions that adhere to the Boltzmann population distribution.[4–6] Due to the attractive optical features of visible light produced by near-IR excitation, many researchers have utilized the LIR technique to deal with RE ion-based upconversion (UC) emission signals.[7–11] One of the most studied areas of LIR optical thermometers right now is the Er^{3+}-doped system.[12] Upon excitation at a wavelength of 980 nm, the numerous ladder-like energy levels of Er^{3+} may produce a bright green UC luminescence, which originates from the $^2H_{11/2} \rightarrow {}^4I_{15/2}$ and $^4S_{3/2} \rightarrow {}^4I_{15/2}$ transitions.[13–16] High-quality LIR-based temperature sensing is made achievable by the exceptional thermal coupling between the $^2H_{11/2}$ and $^4S_{3/2}$ levels.[17] The thermally coupled levels of Er^{3+} are separated by an energy gap of ~800 cm^{-1}, which falls in the ideal range of 200–2000 cm^{-1}, in comparison to other lanthanide ions. Despite the extensive research on optical thermometers based on Er^{3+}, there is still plenty of opportunity to enhance their thermometric sensitivity, detection range, and other critical performance parameters. Moreover, optical thermometers based on TCELs have low sensitivity since they are dependent on their energy difference (ΔE), which falls in the range of 200–2000 cm^{-1}. Consequently, researchers are currently explor-

---

Energy and Environment Unit, Institute of Nanoscience and Technology (INST), Mohali, Punjab, 140306, India. E-mail: naidu245@gmail.com, sanyasinaidu@inst.ac.in

† Electronic supplementary information (ESI) available: Crystal structure, elemental mapping, O 1s photoelectron spectra, emission–excitation contour plots, and photoluminescence spectra in the visible region, energy transfer efficiency, excited state decay curves, as well as lattice parameters and lifetime values. See DOI: **https://doi.org/10.1039/d3nr06401h**

ing the utilization of two separate NTCELs of RE ions in upconverting luminescent materials to address this limitation and enhance their temperature-sensing capacity.

Members of the vanadate-based phosphor group are good examples of materials with great thermal stability along with low phonon energy, allowing luminescence based on RE ions.[18–20] The inclusion of the pyrovanadate group is an important benefit of $Ba_2V_2O_7$-based phosphors over other vanadate or non-oxygen matrices, since they may exhibit exceptionally effective broadband luminescence in the visible light domain, making them suitable for use in lighting applications owing to their impressive color rendering capabilities.[21] There are some reports on pyrovanadate-based nanomaterials that focus on their dielectric and luminescence properties as well as on their different synthesis routes.[22–27] However, there is no approach towards their application in optical thermometers to date.

The present study utilized a citrate-assisted sol–gel technique to synthesize Er^{3+}-doped $Ba_2V_2O_7$-based (BVO) phosphors. The spectral properties of these as-synthesized phosphors were investigated under UV as well as NIR light. Temperature-dependent upconversion luminescence properties were studied, and also the possibility of their application for LIR-based dual-mode temperature sensing.

2. Experimental procedure

2.1. Chemicals required

$Ba(NO_3)_2$ (>99%) and V_2O_5 (>98%) were procured from Merck. $Er(NO_3)_3 \cdot 5H_2O$ (>99.9%) was obtained from Thermo Scientific chemicals. Anhydrous citric acid (>99.5%) and concentrated HNO_3 (~69%) were purchased from Merck.

2.2. Synthesis of $Ba_2V_2O_7$:Er^{3+} nanomaterials

A citrate-gel technique was used to synthesize BVO nanoparticles doped with x at.% Er^{3+} (x = 0.01–0.15). Stoichiometric quantities of $Er(NO_3)_3$, $Ba(NO_3)_2$, and V_2O_5 were weighed following the chemical formula and mixed in a beaker with 50 mL of *aqua dest*. To the above mixture, 2 mL of conc. HNO_3 was added to facilitate the dissolution of V_2O_5. Subsequently, while maintaining a molar ratio of 2 : 1 between citrate and metal ions, a sufficient amount of citrate was introduced to the mixture in order to serve the role of chelating agent. Stirring was done at 363 K over a hot-plate stirrer until the formation of a wet gel (~6 hours). The wet gel is then subjected to drying at 453 K for 12 hours. The resulting xerogel was ground in a mortar after being preheat-treated at 823 K for 5 hours. Finally, the white BVO powder was calcined for 3 hours at 1173 K before processing.

2.3. Characterization

A Bruker D8 Advance X-ray diffractometer was utilized to acquire X-ray diffraction (XRD) patterns. The purpose of these measurements was to examine the crystal phase of the powdered materials generated, within the scanning range of 10°–70°. The crystal structure viewing was done through VESTA software. The nanomaterials underwent morphological characterization by the utilization of a JEOL JSM-7610F Plus field-emission scanning electron microscope, which was aided by energy-dispersive X-ray spectroscopy (EDS). Specifically, a JEOL JEM 2100 Plus transmission electron microscope (200 keV, 0.14 nm resolution) was employed for this purpose. The experimental setup involved the utilization of an Agilent Cary 5000 spectrophotometer to obtain UV-visible-NIR diffuse reflectance spectra (DRS). The photoluminescence (PL) properties were examined using a Horiba Jobin–Yvon Fluorolog 3–221 fluorometer having a 450 W xenon lamp and a visible as well as an NIR photomultiplier tube (PMT) along with an external assembly consisting of a 980 nm CW laser diode.

For temperature-dependent PL experiments, 10 mg of the sample was mixed with a few drops of ethanol to make a slurry. For film formation, this slurry was further dropcast onto a quartz slide and left to dry under ambient conditions. This dropcast sample was used for PL measurements at temperatures ranging from 275 to 650 K using a VPF-800 Janis cryostat with a Lake Shore Model 335 temperature controller.

3. Results and discussion

3.1. Structural and morphological studies

To examine the impact of different concentrations of Er^{3+} dopant on the photoluminescence properties of this particular material, a series of nanoparticles with varied Er^{3+} concentrations ranging from 1 to 15 at% with respect to the Ba^{2+} ions were utilized. BVO:Er^{3+} nanoparticles crystallizing in the triclinic phase with a $P\bar{1}(2)$ space group were generated because of the proposed easier approach. As is apparent in Fig. 1, all the diffraction reflections conform to the reference data (PDF

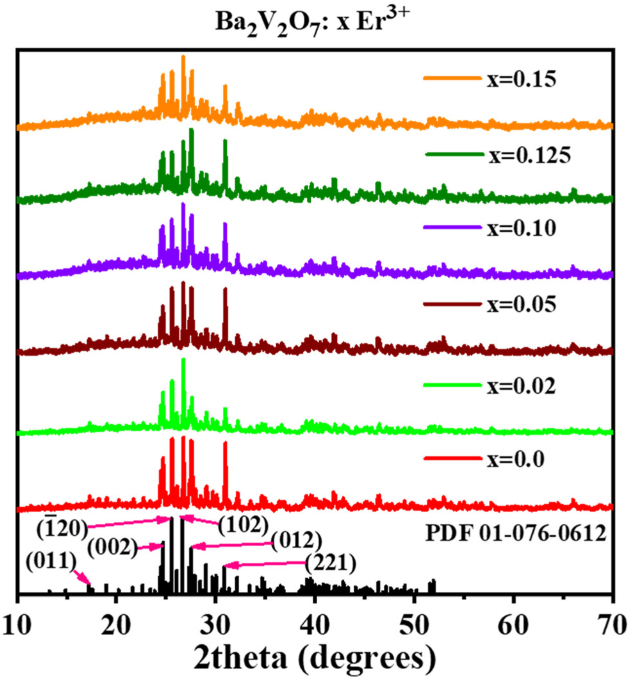

Fig. 1 XRD patterns of $Ba_2V_2O_7$ and its Er^{3+}-doped nanomaterials.

01-076-0612), with no extra peaks indicating the non-existence of another phase or by-products. A schematic of the $Ba_2V_2O_7$ crystal structure is shown in Fig. S1† and the lattice parameters are shown in Table S1 of the ESI.† With the increment in the concentration of Er^{3+}, the lattice parameters decrease, leading to the conclusion that the Er^{3+} is substituting for the Ba^{2+} site, since Er^{3+} is smaller than Ba^{2+}. The crystallite size of the as-prepared phosphors was calculated using the Scherrer equation.[28] The computed crystallite size (D) of the nanomaterials falls within the range of 75–90 nm. High-resolution XPS spectra of undoped BVO and BVO:0.125 Er^{3+} samples demonstrate that oxygen vacancies are present in both the samples and their amount is higher in case of Er^{3+}-doped samples, which show charge compensation due to the doping of Er^{3+} in the Ba^{2+} site (Fig. S2 of the ESI†).

In addition, the BVO host matrix as well as Er^{3+}-doped BVO materials show sheet-like morphology as is evident from FE-SEM and TEM images displayed in Fig. 2(a and b). Fig. 2(c) exhibits the HR-TEM picture, which reveals distinct lattice fringes. The calculated d-spacing of 0.36 nm corresponds to the (002) main plane, providing conclusive evidence for the crystalline structure of the specimen. The dot pattern observed in the selective area electron diffraction (SAED) image (Fig. 2(d)) provides evidence that the particles under investigation possess a single structural phase. Fig. S3 of the ESI† depicts the estimated composition of all the elements present in undoped BVO as per EDS and the mapping of elements, which convey and verify the consistent dispersal of constituent elements throughout the analysed sample.

3.2. Optical properties

DRS spectra of undoped and Er^{3+}-doped $Ba_2V_2O_7$ nanosheets are recorded in the UV-visible-NIR region and presented in Fig. 3. The undoped sample shows broad absorption in the UV range, spanning from 200 to 400 nm with two shoulders. This is attributed to the optical absorption of the vanadate group due to ligand-to-metal charge transfer (LMCT), and can be

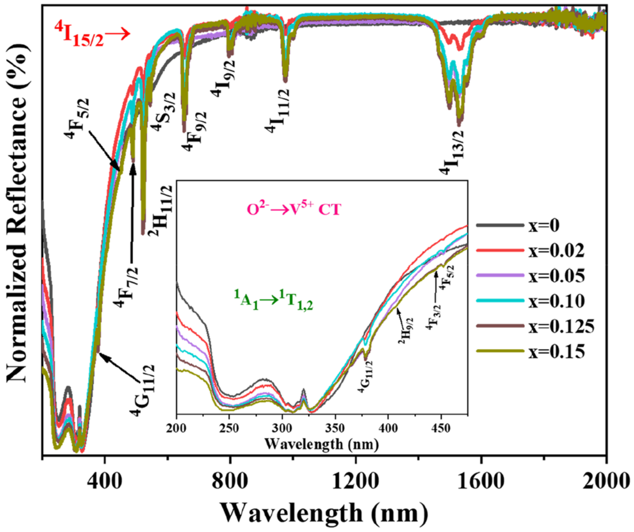

Fig. 3 UV-visible-NIR DRS of $Ba_2V_2O_7$:xEr^{3+} nanomaterials.

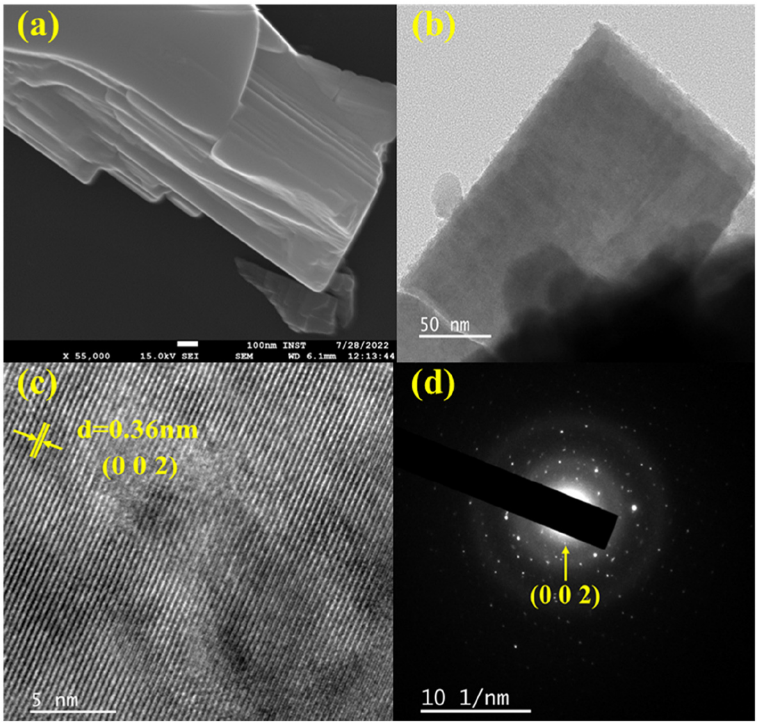

Fig. 2 (a) Field-emission SEM, (b) TEM, (c) HR-TEM, and (d) electron (SAED) diffraction images of undoped $Ba_2V_2O_7$ sheets.

explained by the charge transfer from O^{2-} 2p orbitals to V^{5+} 3d orbitals in the tetrahedral $VO_4{}^{3-}$ symmetry group. This absorption is frequently linked to the transfer of excited electrons from the ground state (GS) $^1A_1$ to the excited states (ES) $^1T_{1,2}$.[25,29] In Er^{3+}-doped samples, apart from the host absorption bands, several sharp peaks in the range from 375–1600 nm are observed, which correspond to the 4f–4f Er^{3+} transitions, *i.e.* absorption from the $^4I_{15/2}$ ground state to $^4I_{13/2}$ (1531 nm), $^4I_{11/2}$ (976 nm), $^4I_{9/2}$ (797 nm), $^4F_{9/2}$ (653 nm), $^4S_{3/2}$ (546 nm), $^2H_{11/2}$ (520 nm), $^4F_{7/2}$ (480 nm), $^4F_{5/2}$ (450 nm) and $^4G_{11/2}$ (380 nm) excited states. The designation of optical absorption bands is based on previous findings.[30]

3.3. Photoluminescence properties

Fig. 4(a) displays the photoluminescence excitation (PLE) spectrum of the BVO host material in the range of 275–400 nm and it has been further deconvoluted using a Gaussian fitting. The spectrum displayed distinct deconvoluted excitation peaks, positioned around 290 and 347 nm. In vanadate compounds, the excitation broadband is typically dictated by the host lattice structure and the vanadate concentration.[31] The deconvoluted excitation spectrum denoted as Ex_1, which is located at a wavelength of 290 nm, is associated with the spin-allowed transition from the $^1A_1$ to the $^1T_2$ electronic state. On the other hand, at the higher excitation band of 347 nm, referred to as Ex_2, is assigned the spin-permitted electronic transition from the $^1A_1$ to the $^1T_1$ state.[22] The electrons in the $^1T_1$ and $^1T_2$ states decay non-radiatively to $^3T_1$ and $^3T_2$ states, from where they decay radiatively to the $^1A_1$ by emitting a very broad emission spanning the wavelength range of 375–675 nm as shown in Fig. 4(b). The $O^{2-} \rightarrow V^{5+}$ charge transfer (CT) is responsible for this broadband emission.[32–34] The difference in energy between the $^3T_1$ and the $^3T_2$ excited state is ~0.3 eV, which means that the two broad peaks overlap and cannot be differentiated from one another. Hence the broad band is deconvoluted into two bands. The compact band (Em_1) at the shorter wavelength positioned at 495 nm refers to the $^3T_2 \rightarrow {}^1A_1$ electronic transition, while the somewhat larger band (Em_2) is imputed to the $^3T_1 \rightarrow {}^1A_1$ electronic transition of the vanadate group, with the band maximum detected at 567 nm (inset of Fig. 4(a)). The relative FWHM values of the Em_1 and Em_2 bands were determined to be 110 and 164 nm, respectively.

To comment on the genesis of luminescence in vanadates, as reported previously, CT in vanadate with T_d symmetry is the cause.[32,35] In general, the $^1A_1 \rightarrow {}^1T_{1,2}$ excitation process is permitted in the ideal T_d symmetry, but the spin selection rule prohibits the $^1T_{1,2} \rightarrow {}^3T_{1,2}$ intersystem crossing, as well as $^3T_{1,2} \rightarrow {}^1A_1$ luminescence processes. In spite of this, the structure of the VO_4 tetrahedron is not identical to that of an ideal tetrahedron. This is because corner-sharing VO_4 dimers induce major distortions in the structure of the VO_4 tetrahedron. As a result, previously disallowed processes are now partially permitted owing to the spin–orbit interaction.

The incorporation of dopants, namely Er^{3+} ions, as seen in Fig. 5(a–d), induces small changes in both the emission profile and intensity of the 513 nm emission spectrum over the series. This phenomenon may be attributed to the sensitivity of Er^{3+} to UV light, resulting in the observation of several energy dips associated with Er^{3+} transitions: $^4F_{7/2} \rightarrow {}^4I_{15/2}$ (488 nm), $^2H_{11/2} \rightarrow {}^4I_{15/2}$ (524 nm, $\mathbf{G_1}$ peak), and $^4S_{3/2} \rightarrow {}^4I_{15/2}$ (545 nm, $\mathbf{G_2}$ peak). Moreover, when the concentration of Er^{3+} increases, the intensity of certain transitions is enhanced due to the improved energy transfer (ET) efficiency between $[V_2O_7]^{4-}$ and Er^{3+}. This is evident in Fig. 5(a) where the host emission profile diminishes and the Er^{3+} emission intensity, as shown in Fig. 5(c), rises with an increase in dopant concentration. The sample doped with x = 0.125 Er^{3+}, on the other hand, has the maximum luminescence intensity. After x = 0.125, the luminescence intensity decreases, which can be ascribed to concentration quenching based on inter-4f cross relaxations. Fig. S4 of the ESI† illustrates contour graphs representing the emission and excitation characteristics of $Ba_2V_2O_7$:Er^{3+} nanomaterials. This resource offers qualitative data on potential excitation wavelengths and the corresponding emis-

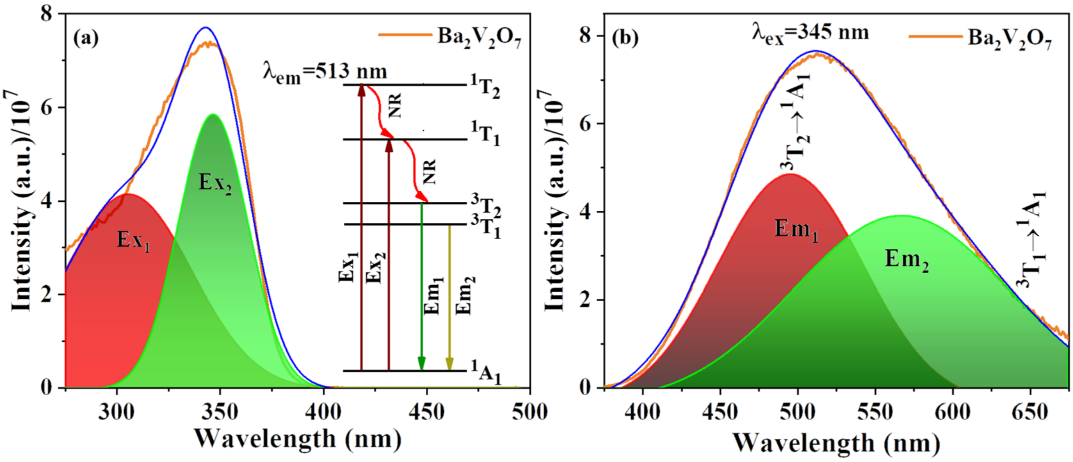

Fig. 4 Gaussian deconvoluted photoluminescence excitation spectra (a) and emission spectra (b) of undoped $Ba_2V_2O_7$ with the inset in (a) depicting the schematic transition processes in the vanadate.

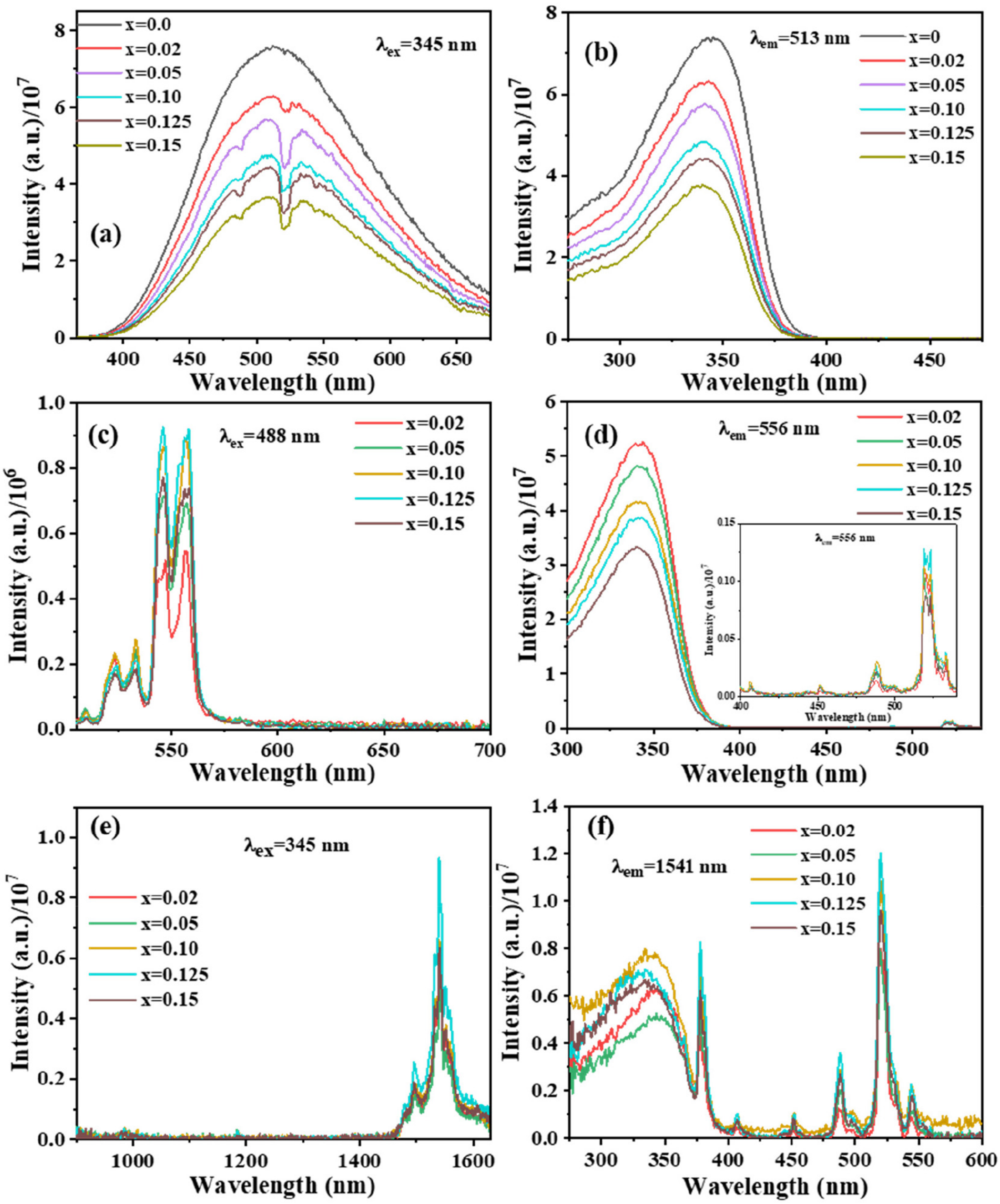

Fig. 5 Photoluminescence spectra excited at (a) 345 nm and (c) 488 nm in the visible region, (e) 345 nm in the NIR region, and excitation spectra monitored at (b) 513 nm, (d) 556 nm, and (f) 1541 nm emission of $Ba_2V_2O_7$:xEr^{3+} (x = 0–0.15).

sion intensities. This observation highlights the significant impact of the excitation wavelength on the relative emission intensities within the visible region.

In addition to examining spectra within the visible range, the emission of the samples doped with erbium was assessed in the near-infrared (NIR) area (Fig. 5(e and f)). The observation of Er^{3+} NIR emission with a 1541 nm peak signifies the involvement of ET from BVO to Er^{3+} ions. Fig. 5(e) displays the NIR emission spectra obtained from Er^{3+}-doped $Ba_2V_2O_7$ nanoparticles when stimulated at 345 nm. There exists a band that is notable for its distinctiveness and is finely split due to the transitions at ${}^4I_{13/2} \rightarrow {}^4I_{15/2}$ (1541 nm). The intensity exhibits an upward trend with increasing concentrations of Er^{3+} up to a threshold of 0.125, beyond which it steadily decreases. The phenomenon of concentration quenching is accountable for the reduction in emission intensity observed above the threshold value of $x = 0.125$. The transfer of energy to the Er^{3+} ion leads to several 4f–4f transitions occurring in the visible as well as NIR regions. However, the diminished intensity of absorption by the host material indicates this phenomenon.

The ET from BVO to Er^{3+} ions can also be elucidated by analysis of the decay lifetime of the 513 nm host emission (λ_{ex} = 345 nm)

(Fig. S5 of ESI†). The bi-exponential decay function provided below effectively modeled the decay curve of the host lattice:

$$I(t) = B_1 \exp\left(-\frac{t}{\tau_1}\right) + B_2 \exp\left(-\frac{t}{\tau_2}\right). \tag{1}$$

The variable $I(t)$ denotes the count at time 't'. The constants τ_1 and τ_2 correspond to the decay lifetime. The average lifetime value may be determined by utilizing the following equation:

$$\tau = \frac{B_1{\tau_1}^2 + B_2{\tau_2}^2}{B_1\tau_1 + B_2\tau_2}. \tag{2}$$

The average lifetime values of the Er^{3+}-doped $Ba_2V_2O_7$ phosphor are tabulated in Table S2 of the ESI.† The decay lifetime of the host lattice can be accurately described by a bi-exponential function. The slower decay observed in this function is attributed to the ET between ${V_2O_7}^{2-}$ and the Er^{3+} dopant. On the other hand, the quicker kinetics observed may be attributed to the surface interaction on the BVO material. When increasing the Er^{3+} concentration in the host lattice, the average lifetime values decrease, which can be attributed to the enhanced energy transfer occurring from the host to Er^{3+} ions. The energy transfer efficiency (η_{ET}) is calculated from the host emission in the presence and absence of Er^{3+} ions and is illustrated in Fig. S6 of the ESI.† It increases when increasing the dopant concentration and reaches a maximum of 52% for the BVO:0.15Er^{3+} sample.

For an examination of the luminescence characteristics of BVO:xEr^{3+} in the process of upconversion, the samples were subjected to illumination using a 980 nm laser diode with a power density of 0.041 W mm^{-2}. The resulting emission spectrum was recorded and is presented in Fig. 6(a). The optimization of luminescence properties is achieved by the manipulation of the percentage of dopant ions (ranging from x = 0.02–0.15) inside the $Ba_2V_2O_7$ host matrix. The emission intensity demonstrates an upward trend as the amount of Er^{3+} ions increases, reaching its peak at x = 0.125, as is evident from the visible and NIR emission spectra, and which is considered the optimal concentration. Subsequently, the emission intensity declines. The observed phenomenon can be ascribed to concentration quenching, namely the heightened inter-Er^{3+} cross-relaxation. The spectral analysis of the UC (upconversion) phenomenon reveals prominent peaks in the green area of the electromagnetic spectrum, namely at wavelengths of 524 nm and 545 nm. These peaks may be imputed to the ${}^2H_{11/2}$ and ${}^4S_{3/2} \rightarrow {}^4I_{15/2}$ transitions of Erbium ions, respectively, which are classified as 4f–4f transitions.

To evaluate the process of UC emission, a mono-log plot was conducted by varying the pump power density to examine

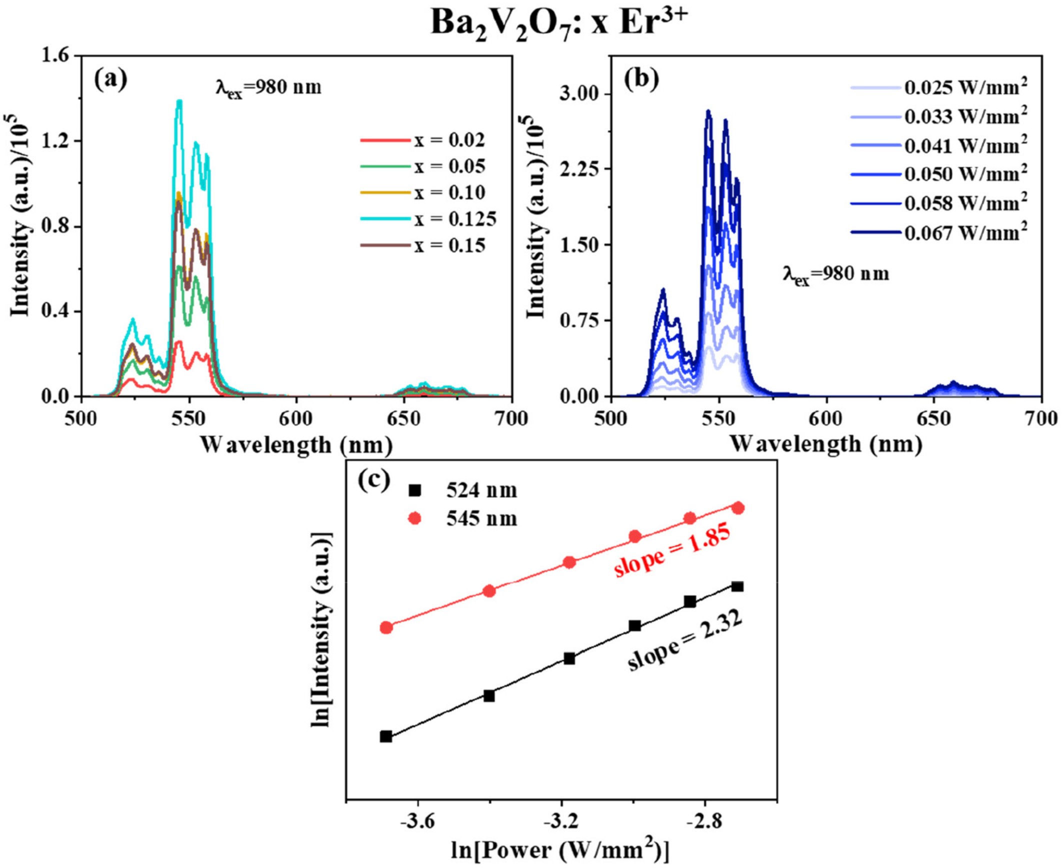

Fig. 6 (a) Upconversion luminescence of doped $Ba_2V_2O_7$:xEr^{3+} phosphors upon excitation with a 980 nm laser. (b) Laser power-dependent upconversion luminescence of $Ba_2V_2O_7$:0.125Er^{3+}. (c) Plot of ln(I) *vs.* ln(P) of $Ba_2V_2O_7$:0.125Er^{3+}.

the connection between upconversion intensity and pump power, as shown in Fig. 6(b and c). This analysis was based on the non-linear relationship expressed as,

$$\text{Intensity} \propto \text{Pump power}^n. \tag{3}$$

In the context of the UC mechanism, the variable '*n*' denotes the quantity of pump (NIR) photons participating in the process. The slope values for emission at 524 nm and 545 nm were determined as 1.85 and 2.32, respectively, by an investigation of the pump power dependency of the BVO:0.125Er^{3+} phosphor (see Fig. 6(c)). Based on the observation that the value of '*n*' just exceeds 2, it may be inferred that the emission in the green area of BVO:Er^{3+} phosphors is attributed to a 2-photon UC mechanism. For the 407 nm blue emission, even though the value of '*n*' is not close to 3, the presence of a 407 nm peak upon excitation with a 980 nm laser, shown in Fig. S7 of the ESI,† is only possible when a 3rd photon governs the UC process, which is explained later on in the section. In addition to the effect of pump power density on the intensity of the sample, it affects the internal temperature of the phosphor. This is known as laser heating and the same phenomenon has been mentioned in Fig. S8 of the ESI.†

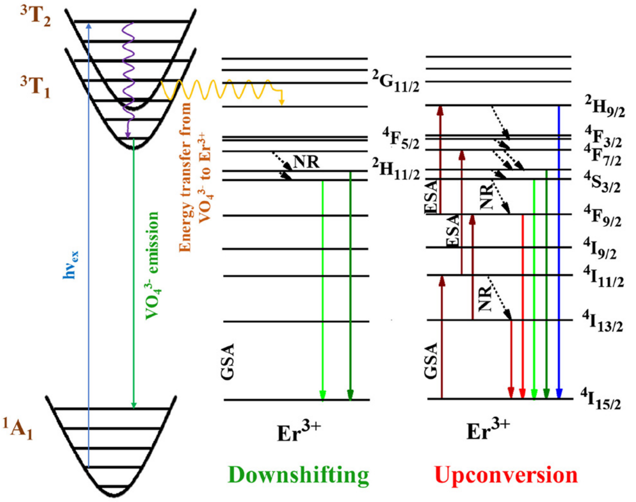

Fig. 7 Schematic of the energy levels of Er^{3+}-doped $Ba_2V_2O_7$, showing the potential transition mechanism.

The energy level diagram depicted in Fig. 7 serves as a visual representation of the hypothetical 980 nm stimulated UC luminescence mechanism seen in erbium-doped barium vanadate (BVO). The primary processes identified as being responsible for the emission of UC include ground and/or excited-state absorption, as well as non-radiative relaxations (NR). The process of single-photon absorption facilitates the transfer of population from the GS $^4I_{15/2}$ to the ES $^4I_{9/2}$. Conversely, two-photon absorption *via* resonance allows the population to be moved to the $^4F_{7/2}$ excited state. There are three lower excited states that the $^2H_{9/2}$ species can spontaneously decay to: $^2H_{11/2}$, $^4S_{3/2}$, and $^4F_{9/2}$. The process of relaxation is accompanied by emission in the green and red spectral regions. The ions inhabiting the ES $^4I_{9/2}$ experience NR relaxation towards the lower ES $^4I_{11/2}$ and $^4I_{13/2}$, leading to the 1541 nm emission. The presence of a third photon can be detected throughout the excitation process from the lower $^4F_{9/2}$ level to the higher $^2H_{9/2}$ level. This excitation results in the subsequent emission of light at a wavelength of 407 nm, as well as further non-radiative relaxations down to the lower energy levels.

3.4. Temperature-sensing studies

Fig. 8(a) illustrates the upconversion spectra of BVO:0.125Er^{3+} at different temperatures when subjected to 980 nm laser irradiation at a power density of 0.041 W mm^{-2}. The temperature investigated spans from 275 to 650 K, the intention being to examine the optical thermometry of rare earth (RE) luminescence. The empirical evidence indicates that the intensity profile of the G_1 and G_2 peaks exhibits a reduction as the temperature increases, but the placements of the bands stay constant. The intensity of the G_2 band, which arises from the $^4S_{3/2}$ energy level, exhibits a decline as temperature increases. Moreover, this decline occurs at a faster rate compared to the intensity drop observed in the red emission ($^4F_{9/2} \rightarrow {}^4I_{15/2}$,

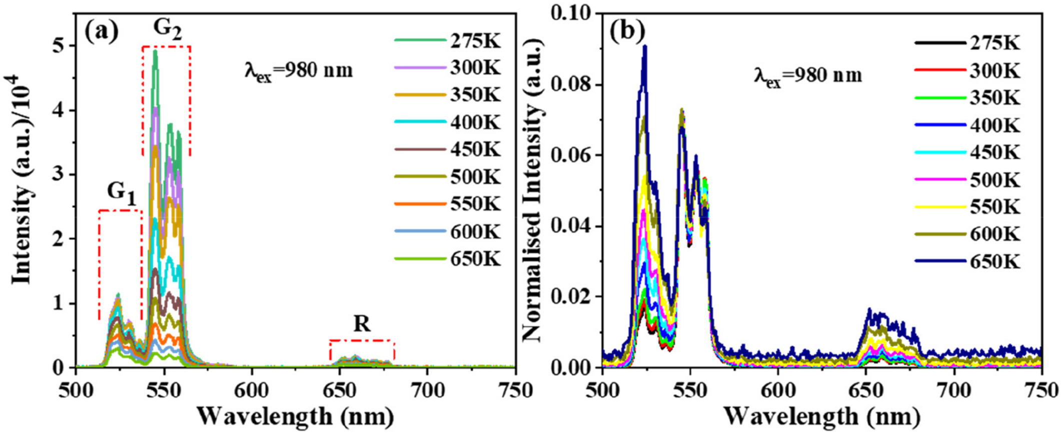

Fig. 8 Temperature-varied (a) UC PL spectra and (b) 551 nm normalized emission spectra of $Ba_2V_2O_7$:0.125Er^{3+}.

denoted by **R**). The phenomenon of thermal quenching is seen due to the NR relaxation from the $^4S_{3/2}$ to $^4F_{9/2}$ levels. As a result of this process, the number of electrons in the $^4F_{9/2}$ level rises while the number of electrons in the $^4S_{3/2}$ level falls. Another factor to consider is the effective utilization of heat activation in promoting the transition of electrons from the $^4S_{3/2}$ to the $^2H_{11/2}$ energy level. As an outcome, the strength of the emission signal from the $^4S_{3/2}$ level is diminished. Fig. 8(b) shows that when temperatures rise, the G_1/G_2 ratio rises. This is because the TCELs and thermal agitation have a small energy gap, thus, the G_1 emission is stronger at higher temperatures.

Fig. 9 and 10 illustrate the graphical representation of the two typical LIR techniques for BVO:0.125Er^{3+} (G_1/G_2 and G_1/R) with respect to temperature. The LIR of TCELs may be described by a Boltzmann distribution:[36]

$$\mathrm{LIR} = B\exp(-C/T) \tag{4}$$

In the above eqn (4), B is denoted as a constant. The variable C is determined by dividing the energy difference (ΔE) by the Boltzmann value (k_B), while T denotes the temperature in Kelvin. The absolute (S_a) and relative (S_r) sensitivities are further derived from the above equation:

$$S_a = \left|\frac{d(\mathrm{LIR})}{dT}\right| = \mathrm{LIR} \times \frac{C}{T^2} \tag{5}$$

$$S_r = 100\% \times \left|\frac{1}{\mathrm{LIR}} \times \frac{d(\mathrm{LIR})}{dT}\right| = \frac{C}{T^2}$$

]Fig. 9(b) displays the variation of S_a and S_r as a function of temperature. At temperatures of 550 K and 275 K, the observed maxima for S_a and S_r are determined as 0.0026 K^{-1} and 1.40% K^{-1}, respectively.

The levels, $^2H_{11/2}$ and $^4F_{9/2}$, are classified as non-thermally coupled energy levels (NTCELs) due to their significant disparity in energy levels, which prevents them from achieving thermal equilibrium. The temperature dependency of the spectral intensity variation in the R band is clearly demonstrated as being identical to that in the G_2 band (see Fig. 8(b)). Consequently, the performance of temperature measurements utilizing the LIR properties of the $^2H_{11/2}$ and $^4F_{9/2}$ energy levels

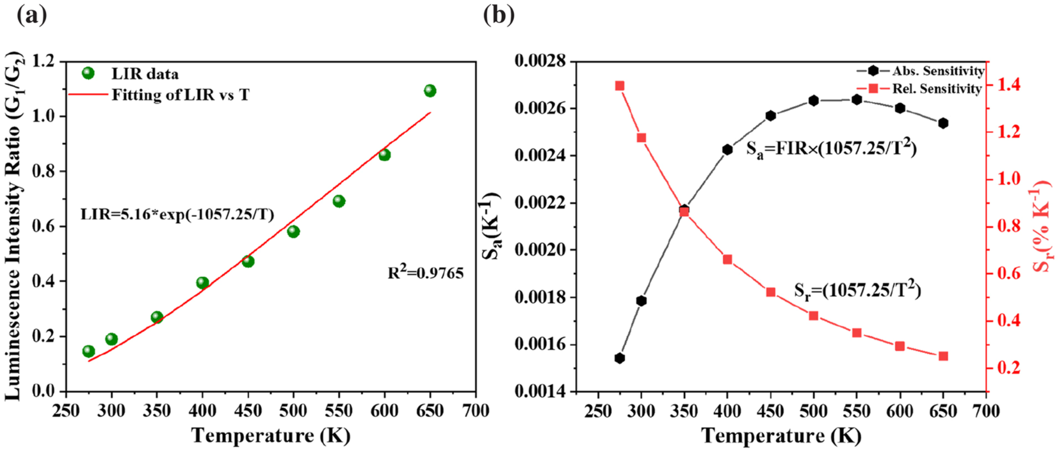

Fig. 9 (a) Temperature dependence of emission intensity ratio and (b) corresponding sensitivities for TCELs of $Ba_2V_2O_7$:0.125Er^{3+}.

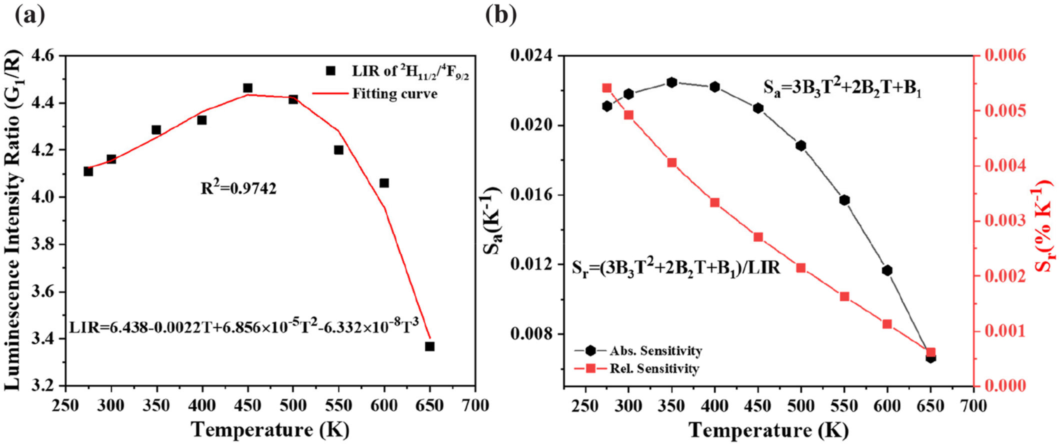

Fig. 10 (a) Temperature dependent luminescence intensity ratio and (b) corresponding sensitivities for NTCELs of $Ba_2V_2O_7$:0.125Er^{3+}.

Table 1 Temperature-sensing characteristics of different upconversion materials

Compounds	Temperature range (K)	S_a (10^{-4} K^{-1})	S_r (% K^{-1})	Ref.
BVO:0.125Er ($^2H_{11/2}/^4S_{3/2}$)	275–650	26	1.40	This work
BVO:0.125Er ($^2H_{11/2}/^4F_{9/2}$)	275–650	230	0.54	This work
$KBi(MoO_4)_2$:Yb/Er	200–550	123	1.82	38
YVO_4:Yb/Er	300–485	116.9	0.86	39
NaY_2F_7:Yb/Er	323–563	36	1.00	40
$BaGdF_5$:Er	300–720	21	1.36	41
$LuVO_4$:Yb/Er@SiO_2 NPs	303–353	115	1.07	42
$BaMoO_4$:Yb/Er	293–553	46	1.08	43
$Sc_2Mo_3O_{12}$:Ho/Yb	303–573	275	—	44
Ca_2MgWO_6:Yb/Er	303–573	82	0.92	45
Bi_5IO_7:Er	303–543	69	1.36	46
$KBaY(MoO_4)_3$:Yb^{3+},Er^{3+}	250–460	130.6	1.80	47
$KBaY(MoO_4)_3$:Yb^{3+},Ho^{3+}	53–293	186	31.45	48

is evaluated. The equation provided can be used to fit the FIR values of the NTCELs (G_1/R):

$$\mathrm{LIR} = B_1 + B_2T + B_3T^2 + B_4T^3 \tag{7}$$

where B_n, n = 1, 2, 3, 4 denotes the fitting constant of the polynomial.[37] The LIR function for the NTCELs in the temperature range of 275–650 K is shown in Fig. 10(a). The absolute and relative sensitivities associated with this function are computed using the aforementioned expression:

$$S_a = \left|\frac{\mathrm{d(LIR)}}{\mathrm{d}T}\right| = B_2 + 2B_3T + 3B_4T^2 \tag{8}$$

$$S_r = 100\% \times \left|\frac{1}{\mathrm{LIR}} \times \frac{\mathrm{d(LIR)}}{\mathrm{d}T}\right| = \frac{1}{\mathrm{LIR}} \times (B_2 + 2B_3T + 3B_4T^2) \tag{9}$$

When the temperature increases, S_r falls, while S_a first rises and subsequently falls. The highest values of S_a and S_r are seen at 350 K and 275 K, respectively, with magnitudes of 0.023 K^{-1} and 0.54% K^{-1}, as depicted in Fig. 10(b).

Luminescent thermometric materials should have a wide temperature range to maximize their application, since this is a key feature of these materials. But in general, the intensity of emission of phosphors diminishes with rising temperature owing to thermal quenching. Consequently, their use in thermometry devices results in significant performance drops when exposed to high temperatures. In correspondence to this, Table 1 presents a comparative analysis of the temperature characteristics shown by several temperature-sensitive materials in various temperature ranges, mostly until 573 K. As is evident, the BVO:0.125Er^{3+} phosphor has good sensitivity in the higher temperature range (until 650 K). With reference to Table 1, the sensitivity shown by the Er^{3+} single-doped phosphor is comparable to or even better than that of the Yb^{3+}, Er^{3+}/Ho^{3+} codoped phosphors.

4. Conclusion

In conclusion, this study represents the first investigation into the thermometric characteristics of BVO:Er^{3+} samples exhibiting favorable upconversion (UC) emission. Triclinic BVO sheet-like nanophosphors are prepared by a citrate-gel technique. The samples exhibit excellent downshifting and upconversion luminescence upon illumination with a UV-vis lamp and 980 nm laser, respectively. The elucidation of the energy level diagram shows that the upconversion process involves a 2-photon mechanism. In the present study, an investigation was conducted on the temperature-sensing capabilities of the LIR technology utilizing the TCELs and NTCELs of Er^{3+} ions. The findings indicated that the highest temperature sensitivity attained was 1.40% K^{-1} and 0.54% K^{-1}, respectively. Due to its enhanced UC luminescence and temperature-sensing characteristics, the synthesized phosphor exhibits potential as a viable option for optical thermometry applications.

Conflicts of interest

There are no conflicts to declare.

Acknowledgements

BSN thanks the DST-SERB, India, for financial support (grant no. CRG/2021/007668); CSIR India (JY), and INST Mohali (SKS) are acknowledged for their Fellowships.

References

1 A. K. Singh, S. K. Singh, B. K. Gupta, R. Prakash and S. B. Rai, *Dalton Trans.*, 2012, **42**, 1065–1072.

2 A. D. Pickel, A. Teitelboim, E. M. Chan, N. J. Borys, P. J. Schuck and C. Dames, *Nat. Commun.*, 2018, **9**, 4907.

3 L. Marciniak, K. Elzbieciak-Piecka, K. Kniec and A. Bednarkiewicz, *J. Chem. Eng.*, 2020, **388**, 124347.

4 A. C. Brandão-Silva, M. A. Gomes, Z. S. Macedo, J. F. M. Avila, J. J. Rodrigues and M. A. R. C. Alencar, *J. Phys. Chem. C*, 2018, **122**, 20459–20468.

5 O. A. Savchuk, J. J. Carvajal, C. Cascales, M. Aguiló and F. Díaz, *ACS Appl. Mater. Interfaces*, 2016, **8**, 7266–7273.

6 Y. Tian, B. Tian, C. Cui, P. Huang, L. Wang and B. Chen, *RSC Adv.*, 2015, **5**, 14123–14128.

7 G. Chen, R. Lei, F. Huang, H. Wang, S. Zhao and S. Xu, *Opt. Commun.*, 2018, **407**, 57–62.

8 H. Lu, H. Hao, Y. Gao, D. Li, G. Shi, Y. Song, Y. Wang and X. Zhang, *Microchim. Acta*, 2017, **184**, 641–646.

9 Z. Cheng, M. Meng, J. Wang, Z. Li, J. He, H. Liang, X. Qiao, Y. Liu and J. Ou, *Nanoscale*, 2023, **15**, 11179–11189.

10 J. D. Kilbane, E. M. Chan, C. Monachon, N. J. Borys, E. S. Levy, A. D. Pickel, J. J. Urban, P. J. Schuck and C. Dames, *Nanoscale*, 2016, **8**, 11611–11616.

11 O. A. Savchuk, J. J. Carvajal, C. D. S. Brites, L. D. Carlos, M. Aguilo and F. Diaz, *Nanoscale*, 2018, **10**, 6602.

12 H. Suo, X. Zhao, Z. Zhang, R. Shi, Y. Wu, J. Xiang and C. Guo, *Nanoscale*, 2018, **10**, 9245–9251.

13 K. C. Liu, Z. Y. Zhang, C. X. Shan, Z. Q. Feng, J. S. Li, C. L. Song, Y. N. Bao, X. H. Qi and B. Dong, *Light: Sci. Appl.*, 2016, **5**, e16136.

14 J. Zhang, Z. Hao, J. Li, X. Zhang, Y. Luo and G. Pan, *Light: Sci. Appl.*, 2015, **4**, 239.

15 B. Dong, D. P. Liu, X. J. Wang, T. Yang, S. M. Miao and C. R. Li, *Appl. Phys. Lett.*, 2007, **90**, 181117.

16 X. Bai, H. Song, G. Pan, Y. Lei, T. Wang, X. Ren, S. Lu, B. Dong, Q. Dai and L. Fan, *J. Phys. Chem. C*, 2007, **111**, 13611–13617.

17 X. Wang, Q. Liu, Y. Bu, C.-S. Liu, T. Liu and X. Yan, *RSC Adv.*, 2015, **5**, 86219–86236.

18 N. Kaczorowska, A. Szczeszak and S. Lis, *Ceram. Int.*, 2021, **47**, 24182–24190.

19 Y. Tian, *J. Solid State Light.*, 2014, **1**, 1–15.

20 Y. Baoxiang, H. Jinyong, Z. Guifang and G. Jike, *Vanadium*, 2021, 395–413.

21 R. Yu, N. Xue, S. Huo, J. Li and J. Wang, *RSC Adv.*, 2015, **5**, 63502–63512.

22 T. Nakajima, M. Isobe, T. Tsuchiya, Y. Ueda and T. Manabe, *Opt. Mater.*, 2010, **32**, 1618–1621.

23 M. R. Joung, J. S. Kim, M. E. Song, S. Nahm and J. H. Paik, *J. Am. Ceram. Soc.*, 2009, **92**, 3092–3094.

24 A. Sharma, M. Varshney, K. H. Chae and S. O. Won, *RSC Adv.*, 2018, **8**, 26423–26431.

25 M. Takahashi, M. Hagiwara and S. Fujihara, *Inorg. Chem.*, 2016, **55**, 7879–7885.

26 N. V. Bharathi, T. Jeyakumaran, S. Ramaswamy and S. S. Jayabalakrishnan, *Mater. Res. Express*, 2019, **6**, 106202.

27 N. Kaczorowska, A. Szczeszak, W. Nowicki and S. Lis, *Polyhedron*, 2022, **223**, 115940.

28 B. D. Cullity, *Elements of x-ray diffraction*, Addison-Wesley Publishing Company, Inc., 1978.

29 R. Yu, M. Yuan, T. Li, Q. Tu and J. Wang, *RSC Adv.*, 2016, **6**, 90711–90717.

30 W. T. Carnall, P. R. Fields and K. Rajnak, *J. Chem. Phys.*, 2003, **49**, 4424.

31 E. Pavitra, G. S. R. Raju, J. Y. Park, L. Wang, B. K. Moon and J. S. Yu, *Sci. Rep.*, 2015, **5**, 1–13.

32 H. Ronde and G. Blasse, *J. Inorg. Nucl. Chem.*, 1978, **40**, 215–219.

33 K. C. Park and S.-I. Mho, *J. Lumin.*, 2007, **122–123**, 95–98.

34 S. Benmokhtar, A. El Jazouli, J. P. Chaminade, P. Gravereau, F. Guillen and D. De Waal, *J. Solid State Chem.*, 2004, **177**, 4175–4182.

35 T. Nakajima, M. Isobe, T. Tsuchiya, Y. Ueda and T. Manabe, *J. Phys. Chem. C*, 2010, **114**, 5160–5167.

36 L. H. Fischer, G. S. Harms and O. S. Wolfbeis, *Angew. Chem., Int. Ed.*, 2011, **50**, 4546–4551.

37 Z. Zheng, J. Zhang, X. Liu, R. Wei, F. Hu and H. Guo, *Ceram. Int.*, 2020, **46**, 6154–6159.

38 S. K. Samal, J. Yadav and B. S. Naidu, *Ceram. Int.*, 2023, **49**, 20051–20060.

39 M. K. Mahata, K. Kumar and V. K. Rai, *Sens. Actuators, B*, 2015, **209**, 775–780.

40 H. L. Gong, X. S. Peng, G. A. Ashraf, F. F. Hu, R. F. Wei and H. Guo, *Ceram. Int.*, 2022, **48**, 4023–4030.

41 F. Hu, S. Lu, Y. Jiang, R. Wei, H. Guo and M. Yin, *J. Lumin.*, 2020, **220**, 116971.

42 G. Xiang, X. Liu, J. Zhang, Z. Liu, W. Liu, Y. Ma, S. Jiang, X. Tang, X. Zhou, L. Li and Y. Jin, *Inorg. Chem.*, 2019, **58**, 8245–8252.

43 R. Lei, X. Liu, F. Huang, D. Deng, S. Zhao, H. Xu and S. Xu, *Opt. Mater.*, 2018, **86**, 278–285.

44 H. Zou, B. Chen, Y. Hu, Q. Zhang, X. Wang and F. Wang, *J. Phys. Chem. Lett.*, 2020, **11**, 3020–3024.

45 Y. C. Jiang, Y. Tong, S. Y. Z. Chen, W. N. Zhang, F. F. Hu, R. F. Wei and H. Guo, *J. Chem. Eng.*, 2021, **413**, 127470.

46 L. Luo, W. Ran, P. Du, W. Li and D. Wang, *Adv. Mater. Interfaces*, 2020, **7**, 1902208.

47 K. Li, D. Zhu and H. Lian, *J. Alloys Compd.*, 2020, **816**, 152554.

48 K. Li, D. Zhu and C. Yue, *J. Mater. Chem. C*, 2022, **10**, 6603–6610.